Available online at www.sciencedirect.com

ScienceDirect

Journal of Sound and Vibration 302 (2007) 577–595

JOURNAL OF SOUND AND VIBRATION

www.elsevier.com/locate/jsvi

Nonlinear dynamics of planetary gears using analytical and finite element models

Vijaya Kumar Ambarisha, Robert G. Parker*

Department of Mechanical Engineering, Ohio State University, 201 W. 19th Avenue, Columbus, OH 43210, USA

Received 9 August 2004; received in revised form 19 October 2006; accepted 27 November 2006
Available online 31 January 2007

Abstract

Vibration-induced gear noise and dynamic loads remain key concerns in many transmission applications that use planetary gears. Tooth separations at large vibrations introduce nonlinearity in geared systems. The present work examines the complex, nonlinear dynamic behavior of spur planetary gears using two models: (i) a lumped-parameter model, and (ii) a finite element model. The two-dimensional (2D) lumped-parameter model represents the gears as lumped inertias, the gear meshes as nonlinear springs with tooth contact loss and periodically varying stiffness due to changing tooth contact conditions, and the supports as linear springs. The 2D finite element model is developed from a unique finite element-contact analysis solver specialized for gear dynamics. Mesh stiffness variation excitation, corner contact, and gear tooth contact loss are all intrinsically considered in the finite element analysis. The dynamics of planetary gears show a rich spectrum of nonlinear phenomena. Nonlinear jumps, chaotic motions, and period-doubling bifurcations occur when the mesh frequency or any of its higher harmonics are near a natural frequency of the system. Responses from the dynamic analysis using analytical and finite element models are successfully compared qualitatively and quantitatively. These comparisons validate the effectiveness of the lumped-parameter model to simulate the dynamics of planetary gears. Mesh phasing rules to suppress rotational and translational vibrations in planetary gears are valid even when nonlinearity from tooth contact loss occurs. These mesh phasing rules, however, are not valid in the chaotic and period-doubling regions.

1. Introduction

Planetary gears are effective power transmission elements where high torque to weight ratios, large speed reductions in compact volumes, co-axial shaft arrangements, high reliability and superior efficiency are required. Example applications are automotive transmissions, tractors, wind turbines, helicopters, and aircraft engines. Gear vibrations are primary concerns in most planetary gear transmission applications, where the manifest problem may be noise or dynamic forces. Noise levels exceeding 110 dB observed in a helicopter cabin are attributed largely to vibration of the planetary gear. Large dynamic forces increase the risk of gear tooth or bearing failure. Kahraman and Blankenship [1,2] performed experiments on a spur gear pair and observed various nonlinear phenomena including gear tooth contact loss, period-doubling and chaos.

---

*Corresponding author. Tel.: +1 614 688 3922; fax: +1 614 292 3163.
E-mail address: parker.242@osu.edu (R.G. Parker).

doi:10.1016/j.jsv.2006.11.028

Tooth separations at large vibrations, which are common in spur–gear pairs, occur even in planetary gears as evident from the experiments by Botman [3].

Planetary gear researchers have developed lumped-parameter models and deformable gear models to analyze gear dynamics. The literature mainly addresses static analysis, natural frequencies and vibration modes, modeling to estimate dynamic forces and responses, and cancellation of mesh forces using the planetary gear symmetry through mesh phasing.

Studies by Cunliffe et al. [4], Botman [5], Hidaka and Terauchi [6], Hidaka et al. [7,8], and Kahraman [9–11] involve planetary gear models to estimate natural frequencies, vibration modes and dynamic forces. Lin and Parker [12,13] present a 2D rotational–translational degree of freedom spur gear model and mathematically show the unique modal properties of equally spaced and diametrically opposed planet systems. All modes can be classified as one of rotational, translational, or planet modes. The sensitivity of natural frequencies and modes to operating speeds and various design parameters are studied by Lin and Parker [14], who also examine natural frequency veering phenomena [15]. Mesh stiffness-induced parametric instability is studied by Lin and Parker [16]. A helical planetary gear model is formulated and the effect of mesh phasing on the dynamics of equally spaced planet systems is investigated by Kahraman [9] and Kahraman and Blankenship [17]. Parker [18] showed the effectiveness of mesh phasing in suppressing certain harmonics of planetary gear vibration modes based on self-equilibration of the dynamic mesh forces at sun–planet and ring–planet meshes. Ambarisha and Parker [19] extended this work to derive design rules to suppress planet mode resonances. A thorough description of the relative mesh phasing between the sun–planet and ring–planet meshes in a planetary gear system is given by Parker and Lin [20]. A nonlinear dynamic planetary gear model is introduced by Kahraman [11] and the effects of various design parameters on the dynamic load sharing of the planets are examined. Velex and Flamand [21] studied the planetary gear dynamics using lumped-parameter model.

In recent years, some researchers have used deformable gear body dynamic models. A unique finite element-contact analysis program is used by Parker et al. [22] to model nonlinear spur gear dynamics. The finite element results compare favorably with experiments. Parker et al. [23] used the same finite element method to examine planetary gear dynamics. Kahraman and Vijayakar [24] studied the effect of ring gear flexibility on the static response of planetary gears using the finite element method. A recent study by Kahraman et al. [25] dynamically analyzes a planetary gear with thin rim using the same finite element method. Yuksel and Kahraman [26] employed this finite element model to study tooth wear and its impact on the dynamic behavior of a planetary gear. These studies use the same commercial finite element tool [27], which is also adopted in this study.

Accurate analytical modeling, including proper mesh phasing relations and detailed characterization of the nonlinear dynamics of planetary gears, is needed to estimate relative gear noise and predict dynamic forces in industrial applications. Little work has been done to characterize the nonlinear effects of tooth separation on planetary gear dynamics. The lack of experimental studies to understand the complex dynamics of planetary gears and the availability of finite element software specialized for gear dynamics motivated the present study. The objectives of this study are to: (a) characterize the complex, nonlinear dynamics of spur planetary gear systems using a unique finite element model, and (b) propose a lumped-parameter analytical model that is validated by comparisons with the finite element results across the range of complicated nonlinear dynamics occurring in the system.

2. Modeling of planetary gear dynamics

2.1. Lumped-parameter analytical model

The 2D planetary gear model developed by Lin and Parker [12], extended to include tooth contact loss, is used. This lumped-parameter, discrete model (Fig. 1(a)) is referred to as the *analytical* model. The gear mesh is modeled as a nonlinear spring with periodically varying stiffness acting along the line of action. All other supports/bearings are modeled as linear springs. The periodically varying mesh stiffness is due to the change in the number of teeth in contact as the gears rotate. Nonlinear tooth mesh separations occur due to large relative vibrations and the presence of backlash between the mating gear teeth [1–3]. Friction forces due to gear teeth contact and other dissipative effects are captured using modal damping.

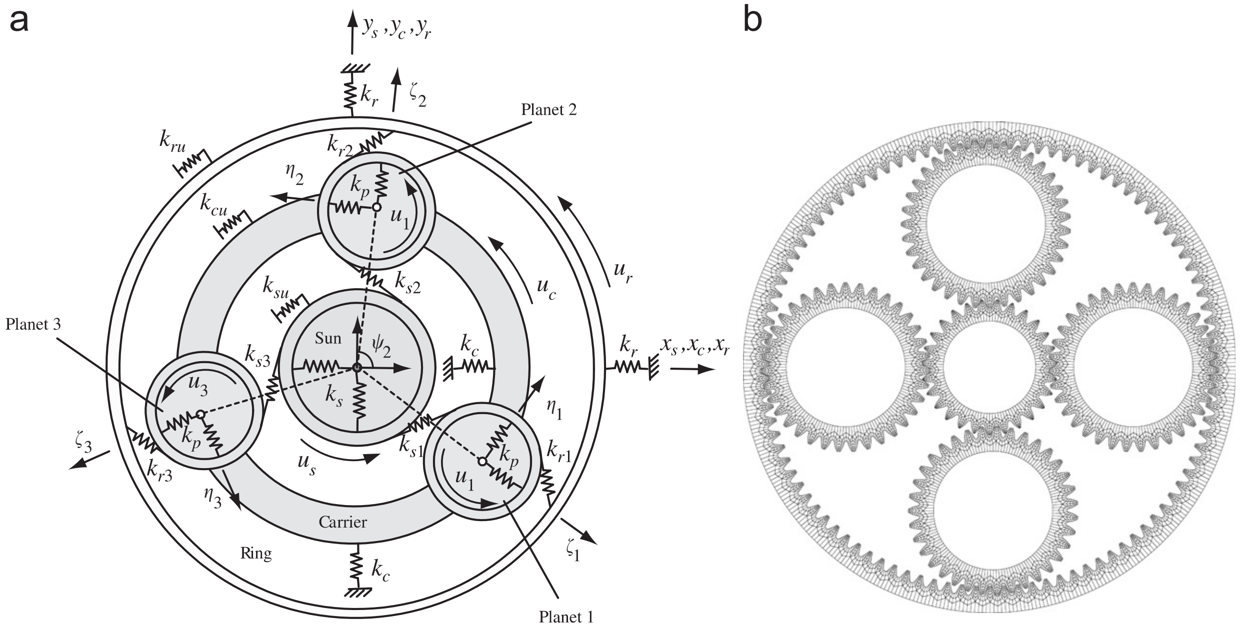

Fig. 1. Planetary gear (a) lumped-parameter analytical and (b) finite element models.

The equation of motion for a spur planetary system with N planets is

$$\mathbf{M}\ddot{\mathbf{x}} + \mathbf{C}\dot{\mathbf{x}} + \mathbf{K}(\mathbf{x}, t)\mathbf{x} = \mathbf{F}(t), \tag{1}$$

where $\mathbf{x} = \left[x_c, y_c, u_c, x_r, y_r, u_r, x_s, y_s, u_s, \zeta_1, \eta_1, u_1, \ldots, \zeta_N, \eta_N, u_N\right]^{\mathrm{T}}$and $\mathbf{F}(t)$ is the force vector of externally applied torques (refer to Ref. [12] for system matrices). Also, x, y represent translations, u is the rotational deflection (rotation in radians times the gear base radii or radius to the planet centers for the carrier), and ζ, η are the planet radial and tangential deflections; c, r, s represent the carrier, ring and sun, respectively, and the subscripts from $1,\ldots,N$ designate the planets. The total number of degrees of freedom is $M = 3N+9$.

The damping matrix $\mathbf{C}$ is obtained from $\mathbf{C} = \mathbf{U}^{-\mathrm{T}}\mathrm{diag}(2\rho_i\omega_i)\mathbf{U}^{-1}$, where ρ_i $(i = 1,\ldots,M)$ are modal damping ratios approximating the material and bearing damping used in the finite element model, and the natural frequencies ω_i and orthonormalized modal matrix $\mathbf{U}$ are from the time-invariant system with average mesh stiffness.

The inertias, gear geometry parameters, natural frequencies, and damping ratios of the various systems analyzed in this paper are given in Tables 1–3.

The nonlinearity from tooth contact loss is incorporated into the stiffness matrix through the sun–planet and ring–planet mesh stiffnesses as

$$k_{jn}(\mathbf{x}, t) = h(\delta_{jn})\hat{k}_{jn}(t), \tag{2}$$

where

$$h(\delta_{jn}) = \begin{cases} 1, & \delta_{jn} > 0, \\ 0, & \delta_{jn} < 0 \end{cases}$$

for $j = s, r$; $n = 1,\ldots,N$, and

$$\begin{aligned} \delta_{sn} &= y_s \cos\psi_{sn} - x_s \sin\psi_{sn} - \zeta_n \sin\alpha_s - \eta_n \cos\alpha_s + u_s + u_n, \\ \delta_{rn} &= y_r \cos\psi_{rn} - x_r \sin\psi_{rn} + \zeta_n \sin\alpha_r - \eta_n \cos\alpha_r + u_r - u_n, \end{aligned}$$

Table 1
Natural frequencies of four different systems analyzed in this study

	System description	Natural frequencies (Hz)
Case 1	3 planets, equally spaced	DT: $\omega_1 = 1846$, $\omega_4 = 4379$
	Rotational system	DE: ω_2, $\omega_3 = 2744$
Case 2	4 planets, diametrically opposed ($\psi_1 = 0$, $\psi_2 = 31\pi/63$)	DT: $\omega_1 = 1925$, $\omega_5 = 4690$
	Rotational system	DE: $\omega_2 = 2593$, $\omega_3 = 2688$, $\omega_4 = 2860$
Case 3	3 planets, equally spaced	T: ω_1, $\omega_2 = 1760$, ω_4, $\omega_5 = 3390$
	Translational–rotational system	R: $\omega_3 = 2095$, $\omega_6 = 5249$
Case 4	4 planets, diametrically opposed ($\psi_1 = 0$, $\psi_2 = 31\pi/63$)	T: $\omega_1 = 1766$, $\omega_2 = 1781$, $\omega_4 = 3326$, $\omega_5 = 3332$
	Translational–rotational system	R: $\omega_3 = 2159$
		P: $\omega_6 = 3580$

Parameters are in Table 2.

Note: DT, distinct mode; DE, degenerate mode; T, translational mode; R, rotational mode; P, planet mode.

Table 2
Data for the planetary gear configurations presented in this work

Gear data	Sun gear	Ring gear	Planet gear (mesh with sun gear)
Number of teeth	27	99	35
Module (mm)	2.8677	2.7782	2.8677
Pressure angle (deg)	24.60	20.19	24.60
Circular tooth thickness at pitch dia. (mm)	4.470	3.124	4.140
Hob tip radius (mm)	1.041	—	0.457
Fillet radius (mm)	—	1.473	—
Base circle dia. (mm)	70.399	258.130	91.257
Root dia. (mm)	70.485	284.150	91.440
Inner dia. (mm)	57.15	—	73.66
Minor dia. (mm)	—	271.73	—
Outer dia. (mm)	84.074	304.800	105.004
	Center distance = 88.89 mm		

System parameters

	Rotational system (cases 1 & 2)			Transl.–rotl. system (cases 3 & 4)		
	Sun	Planet	Carrier	Sun	Planet	Carrier
I/r^2 (kg)	3.11	4.89	24.80	1.56	2.46	24.80
Mass (kg)	—	2.64	—	1.64	1.33	21.82
Base dia. (mm)	70.40	91.26	177.8	70.40	91.26	177.80
Bearing stiff. (N/m)		—			$k_c = k_p = k_s = 2.19\text{e}9$	
Mesh stiff. (N/m)				From Fig. 2		
Pressure angle (deg)				$\alpha_s = 24.6$, $\alpha_r = 20.19$		

Table 3
Damping ratios corresponding to respective natural frequencies for different cases in Table 1

	Damping ratios (%)
Case 1	$\rho_1 = 2.46$, $\rho_2 = \rho_3 = 1.10$, $\rho_4 = 2.10$
Case 2	$\rho_1 = 2.14$, $\rho_2 = \rho_3 = \rho_4 = 1.36$, $\rho_5 = 1.63$
Case 3	$\rho_1 = \rho_2 = 0.82$, $\rho_3 = 1.07$, $\rho_4 = \rho_5 = 0.70$, $\rho_6 = 1.53$ ($\rho_{7-14} \approx 3$–5)
Case 4	$\rho_1 = \rho_2 = 1.25$, $\rho_3 = 1.00$, $\rho_4 = \rho_5 = 0.84$, $\rho_6 = 0.67$ ($\rho_{7-17} \approx 3$–5)

where $\widehat{k}_{jn}$ is the linear, periodically varying mesh stiffness, δ_{sn} and δ_{rn} are the compressive deflections in the sun–planet and ring–planet mesh springs, α_s and α_r are the sun–planet and ring–planet operating pressure angles, ψ_n is the circumferential position of planet n around the sun ($\psi_1 = 0$), $\psi_{sn} = \psi_n - \alpha_s$ and $\psi_{rn} = \psi_n + \alpha_r$. Mesh phase relations are enforced according to Parker and Lin [20].

A purely *rotational* model can be reduced from the above rotational–translational system by removing the translations of the components. The rotational model allows mesh model verification isolated from the effects of bearing deflections. The equation of motion for a *rotational* model with N planets is [19]

$$\mathbf{M}\ddot{\mathbf{x}} + \mathbf{C}\dot{\mathbf{x}} + \mathbf{K}(\mathbf{x}, t)\mathbf{x} = \mathbf{F}(t), \tag{3}$$

where $\mathbf{x} = [u_c, u_r, u_s, u_1, \ldots, u_N]^{\mathrm{T}}$.

The inertia matrix,

$$\mathbf{M} = \mathrm{diag}(I_c/r_c^2 + Nm_p, I_r/r_r^2, \underbrace{I_p/r_p^2, \ldots, I_p/r_p^2}_{N}),$$

where I_j for $j = c$, r, s, p (p represents planet gear) are the moments of inertia, r_j are base radii of the gears or radius of the carrier, and m_p is the mass of a planet. The damping matrix $\mathbf{C}$ is obtained as for a rotational–translational model. The stiffness matrix

$$\mathbf{K}(\mathbf{x}, t) = \mathbf{K}_b + \mathbf{K}_m(\mathbf{x}, t),$$

where

$$\mathbf{K}_b = \mathrm{diag}(k_{cu}, k_{ru}, k_{su}, 0, \ldots, 0)$$

k_{ju} for $j = c$, r, s is the torsional bearing stiffness, and the mesh stiffness matrix $\mathbf{K}_m$ from Ref. [19] is

$$\mathbf{K}_m = \begin{pmatrix} \sum(\widetilde{k}_{sn}\cos\alpha_s + \widetilde{k}_{rn}\cos\alpha_r) & -\sum\widetilde{k}_{rn} & -\sum\widetilde{k}_{sn} & \widetilde{k}_{r1} - \widetilde{k}_{s1} & \widetilde{k}_{r2} - \widetilde{k}_{s2} & \cdots & \widetilde{k}_{rN} - \widetilde{k}_{sN} \\ & \sum k_{rn} & 0 & -k_{r1} & -k_{r2} & \cdots & -k_{rN} \\ & & \sum k_{sn} & k_{s1} & k_{s2} & \cdots & k_{sN} \\ & & & k_{r1} + k_{s1} & 0 & \cdots & 0 \\ & \text{symmetric} & & & \ddots & \cdots & \vdots \\ & & & & & & k_{rN} + k_{sN} \end{pmatrix}, \tag{4}$$

where $\widetilde{k}_{sn} = k_{sn}(t)\cos\alpha_s, \quad \widetilde{k}_{rn} = k_{rn}(t)\cos\alpha_r$.

Note in prior studies [10,16] the factors of $\cos\alpha_s$ and $\cos\alpha_r$ in their rotational model stiffness matrix were mistakenly omitted. Nonlinearity from tooth contact loss is introduced into the sun–planet and ring–planet mesh stiffnesses based upon whether the mesh springs are in compression or not

$$k_{jn}(\mathbf{x}, t) = h(\delta_{jn})\hat{k}_{jn}(t), \tag{5}$$

where

$$h(\delta_{jn}) = \begin{cases} 1, & \delta_{jn} > 0, \\ 0, & \delta_{jn} < 0 \end{cases}$$

for $j = s$, r; $n = 1,\ldots,N$, and

$$\delta_{sn} = -u_c\cos\alpha_s + u_s + u_n,$$
$$\delta_{rn} = -u_c\cos\alpha_r + u_r - u_n.$$

2.2. Finite element model

Unique commercial finite element-contact analysis software (Calyx [27]) specialized for gear dynamics is used to model the planetary gears. This software uses a combined surface integral and finite element solution

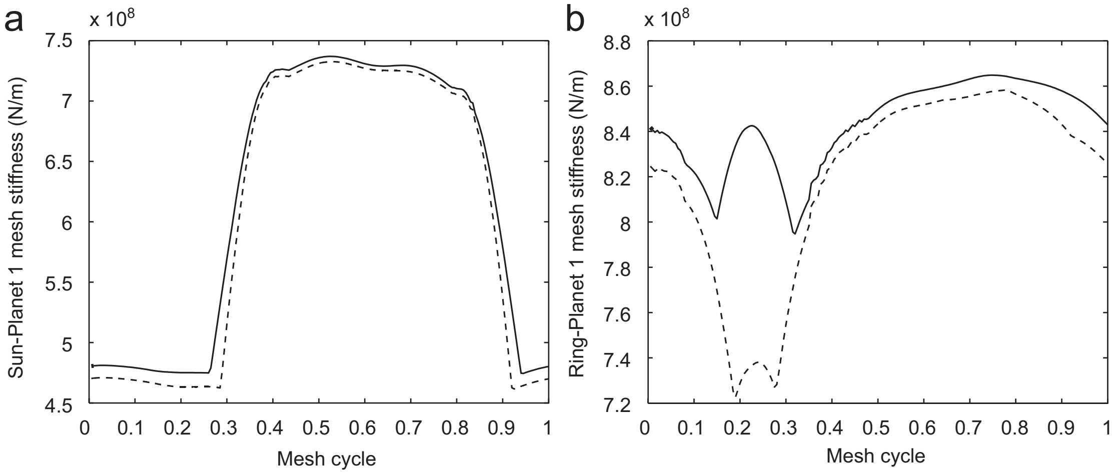

Fig. 2. Mesh stiffness variation from finite element static analysis of isolated gear pairs (a) sun–planet 1 mesh and (b) ring–planet 1 mesh, for the three planets (cases 1 and 3) and four planets (cases 2 and 4) systems for an input torque of 1130 N m (10,000 Lbf in) on the sun: (—) 3 planets case and (- - -) 4 planets case.

approach developed by Vijayakar [28] and Vijayakar et al. [29]. A description of the gear dynamics finite element formulation is given by Parker et al. [22,23]. The efficiency of the formulation dramatically reduces the number of finite elements and enables dynamic analysis with practically feasible run times.

The finite element model does not require any external specification of the periodically varying mesh stiffness or static transmission error to excite the dynamics. The only inputs, in addition to the gear geometry and material properties, are the input torque and the speed of the gears. Mesh stiffness variation due to the change in the number of teeth in contact, corner contact due to the elastic deformations of the gear teeth, tooth contact loss, and gear body elastic compliance are all intrinsically modeled in the finite element model. Transmission error is a computed output; there is no need to invoke approximations with static transmission error as an excitation. This model significantly reduces the assumptions needed to model the complex dynamic mesh forces.

Reference frames are attached to each component, and these rotate according to nominal trajectories from the rigid body kinematics of planetary gears. The calculated rotational and translational component vibrations are the deflections of the bodies from these nominal kinematic positions (i.e., dynamic transmission error and translational motions on bearings). Bearings are modeled with 3×3 stiffness matrices. Viscous bearing damping is included by a 3×3 damping matrix between the connecting bodies.

Small values of material damping coefficients α and β are introduced in the finite element models to remove numerical instabilities in the solution method. The Rayleigh damping model used here assumes that the damping of a finite element is proportional to the mass ($\mathbf{M}_{\mathrm{fe}}$) and stiffness ($\mathbf{K}_{\mathrm{fe}}$) of the element, i.e., $\mathbf{C}_{\mathrm{fe}} = \alpha\mathbf{M}_{\mathrm{fe}} + \beta\mathbf{K}_{\mathrm{fe}}$. The viscous bearing damping and the material damping coefficients are selected such that the damping ratios at the vibration modes of interest are less than 3%. These values are comparable to the 1% value that Blankenship and Kahraman [2] estimated for their experiments on a spur gear pair.

The finite element model of an example system with four planets is shown in Fig. 1(b). The carrier (not shown) is modeled as a lumped inertia. The gear geometry data is given in Table 2. All the planetary gear configurations analyzed in this study have the same gears and carrier. The exterior circle of the ring gear and the interior bores of the sun and planet gears are constrained to remain circular. In some applications, the gear bodies, especially the ring gear, may deform elastically into non-circular shapes, requiring an extension of the present analytical model [30]. The outer ring gear circle is rigidly fixed in all systems considered. The constant input torque is applied at the sun gear. The carrier rotational vibration is constrained to zero, i.e., the carrier always rotates according to its nominal kinematic position, which removes the rigid body mode.

2.2.1. Mesh stiffness variation from the finite element model

Because of the continuous gear rotation, the gear meshing is periodic at the mesh frequency, which is the same at all meshes in a single stage planetary gear. The mesh frequency ω_m for a system with fixed ring is

$$\omega_m = \frac{Z_s Z_r}{Z_s + Z_r}\omega_s, \tag{6}$$

where ω_s is the sun speed, and Z_s, Z_r are the numbers of teeth on the sun and ring gears, respectively.

The mesh stiffness variation of a sun–planet mesh is obtained from static finite element analysis of an isolated sun–planet pair. The gear pair has rigid bearings to isolate mesh stiffness from any bearing deflections. The planet is constrained not to rotate and the torque $T_s = T/N$ is applied on the sun, where T is the sun torque of the planetary system. From the calculated transmission error $u_s = r_s\theta_s$, the mesh stiffness $\hat{k}_{s1}$ at a particular mesh position is $\hat{k}_{s1} = T_s/(r_s u_s)$. This calculation is repeated at multiple steps within a mesh cycle. A similar process is used for the ring–planet mesh. Mesh stiffness variations of the sun–planet 1 and ring–planet 1 meshes calculated for the example systems in Table 1 at the sun input torque of 1130 N m are shown in Fig. 2. Differences for the three and four planet cases result due to the change in mesh forces as a result of load sharing among planets for the same input torque. In particular, the large variation in the ring–planet mesh stiffness in Fig. 2(b) between the three and four planet cases is due to corner contact at higher mesh forces in the three planet case. These figures can be translated into time-varying mesh stiffness histories when viewed as variations over a period $t_0 \rightarrow t_0 + T_m$.

Table 4
Mesh phasing rules to excite various harmonics (l) of modal responses in equally spaced and diametrically opposed planet systems for both rotational–translational and purely rotational systems (from Refs. [18,19])

	Rotational–translational system			Purely rotational system	
	Planet mode	Rotational mode	Translational mode	Degenerate mode	Distinct mode
Equally spaced planets, $k_l = \mathrm{mod}(lZ_s/N)$	$k_l \neq 0, 1, N-1$	0	$1, N-1$	$k_l \neq 0$	0
Diametrically opposed planet pairs, lZ_s	Even ($N = 4$); all ($N \geqslant 6$)	Even	Odd	All	Even

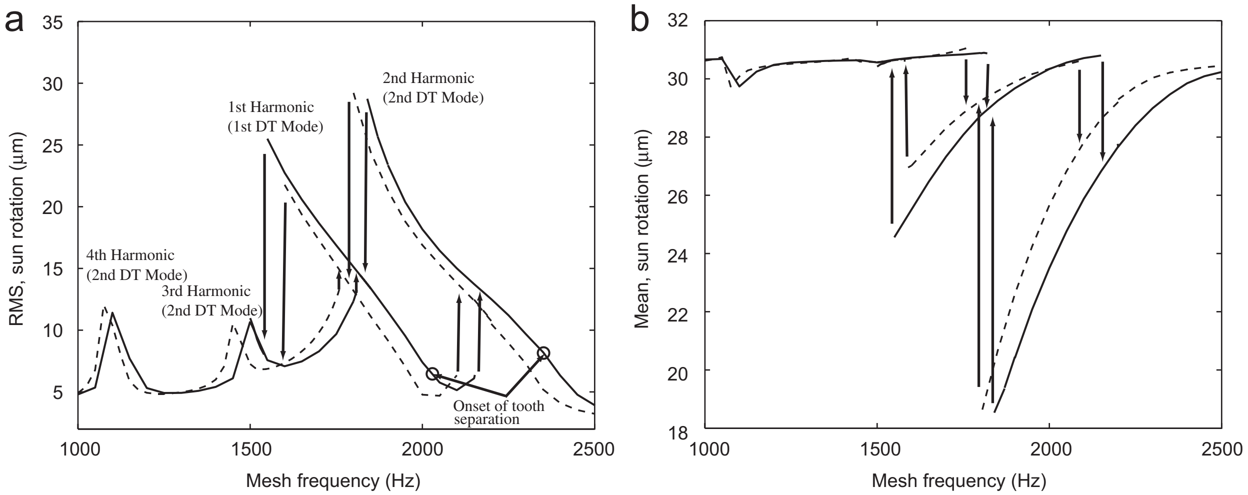

Fig. 3. Steady state (a) rms values (mean removed), and (b) mean values of sun rotation for increasing and decreasing speeds in finite element and analytical models for case 1 (*note*: DT Mode—distinct mode): (—) FE model and (- - -) analytical model.

A relative mesh phase γ_{rs} exists between sun–planet and ring–planet meshes for a given planet (measured from pitch points) [20]. In the present analysis the beginning mesh cycle points (and all other points) in the isolated sun–planet 1 and ring–planet 1 analyses of Fig. 2(a) and (b) correspond to an identical planet 1 position in the assembled planetary gear. Thus, the mesh stiffnesses in Fig. 2 calculated from the isolated sun–planet 1 and ring–planet 1 gear pairs automatically contain the relative mesh phase between the sun–planet 1 and ring–planet 1 meshes. The mesh stiffness of all other sun–planet and ring–planet meshes are obtained from the mesh phase relations [18,20]

$$\hat{k}_{sn}(t) = \hat{k}_{s1}(t - \gamma_{sn}T_m), \quad \hat{k}_{rn}(t) = \hat{k}_{r1}(t - \gamma_{rn}T_m), \tag{7}$$

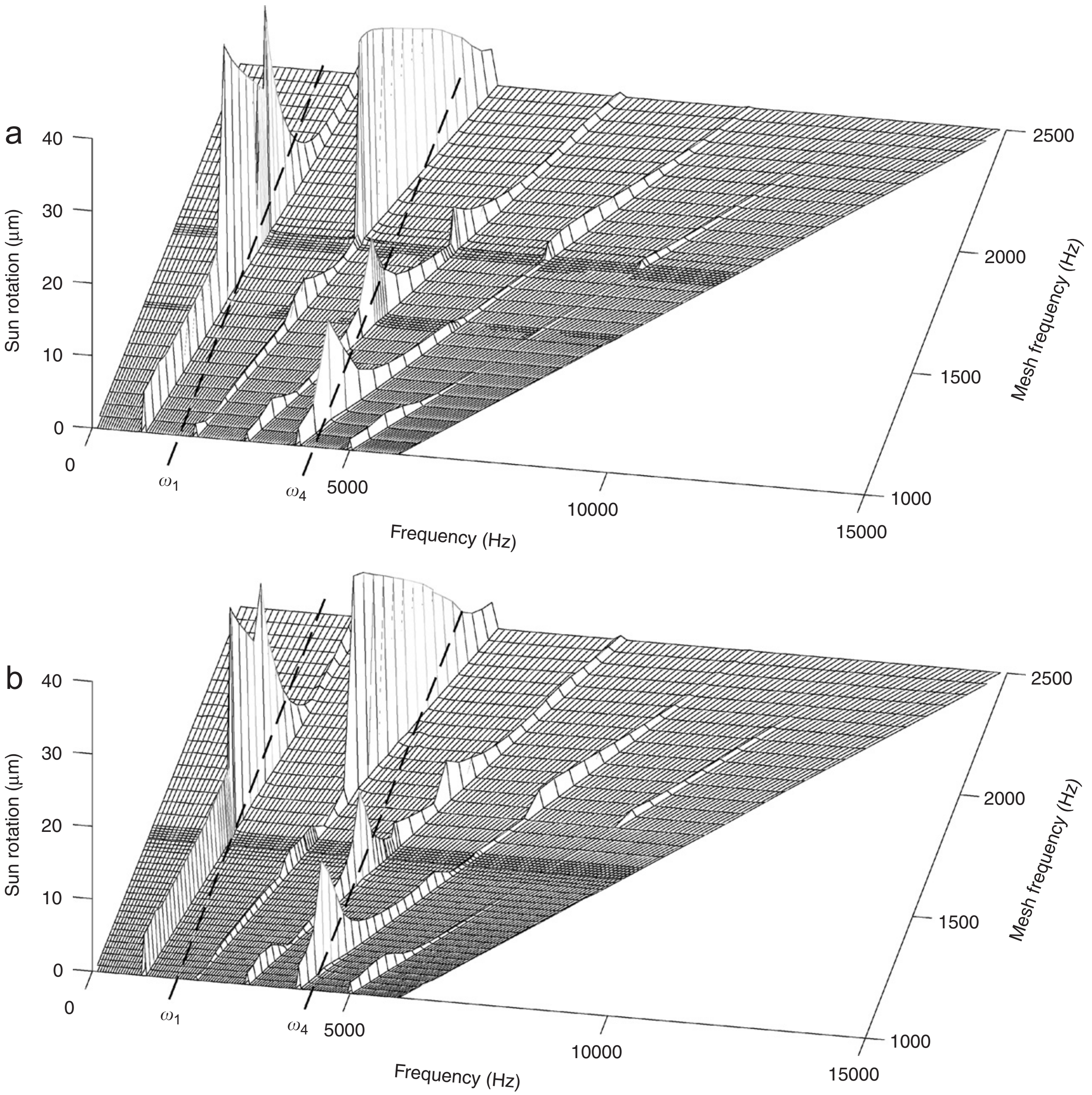

Fig. 4. Waterfall spectra of sun rotation for decreasing speeds in (a) finite element model and (b) analytical models of case 1.

where $\hat{k}_{sn}$, $\hat{k}_{rn}$ are the planet n mesh stiffnesses with the sun and ring, respectively, γ_{sn}, γ_{rn} are the sun–planet n and ring–planet n mesh phases, and $T_m = 2\pi/\omega_m$ is the mesh period. The mesh phases are

$$\gamma_{sn} = \pm Z_s \psi_n, \quad \gamma_{rn} = \mp Z_r \psi_n, \tag{8}$$

where the upper and lower signs are for systems with clockwise and counter-clockwise planet rotations, respectively.

3. Nonlinear dynamic response of planetary gears

In the present study the dynamics of four planetary gear configurations are analyzed. The system parameters are given in Tables 1–3. The gear teeth are perfect involutes. The ring gear is fixed in the present study, although fixed sun and fixed carrier cases can be treated similarly. The carrier is constrained to have zero rotational vibration, corresponding to a very high inertia of the output element. The natural frequencies of these systems are given in Table 1. The rotational systems in cases 1 and 2 have two sets of natural frequencies and modes: distinct modes in which all the components of the system rotate, and degenerate modes in which the sun, ring and carrier do not rotate, only the planets rotate [16]. The rotational–translational systems (cases 3 and 4) in general have three sets of natural frequencies and modes: rotational modes, translational modes and planet modes [12]. Planet modes exist only for systems with number of planets $N > 3$.

Numerical integration is used for both models. For speed sweeps in the analytical model, speed is varied in sharp steps by changing the mesh period T_m. The final steady-state response at a particular speed is used as the initial condition for the next speed. Eq. (1) is solved by using a fourth-order Runge–Kutta integration method. In order to capture a sufficient number of mesh frequency harmonics in the response spectra, 100 time steps per mesh cycle are selected. The transient region, which is discarded at each speed change, extends for 50 mesh cycles before recording the steady-state solution. To obtain sufficient frequency resolution in the response spectra, the steady-state response is recorded for 20 mesh cycles. For speed sweeps in the finite element model, speed is varied continuously in ramp changes between steady values. The ramp rate, transient time, and other numerical parameters for the finite element model are carefully selected to achieve numerical stability, convergence of solutions, and reduction in computation time with minimal effect on the computed results.

Before looking at the dynamic responses, it is important to understand how mesh phasing excites or suppresses certain harmonics of the rotational, translational and planet mode responses. Mesh phasing rules are derived based on the symmetry of planetary gears and periodicity of the mesh forces [17–20]. These mesh phasing rules are summarized in Table 4. If a rotational (or translational mode) is excited in a given harmonic

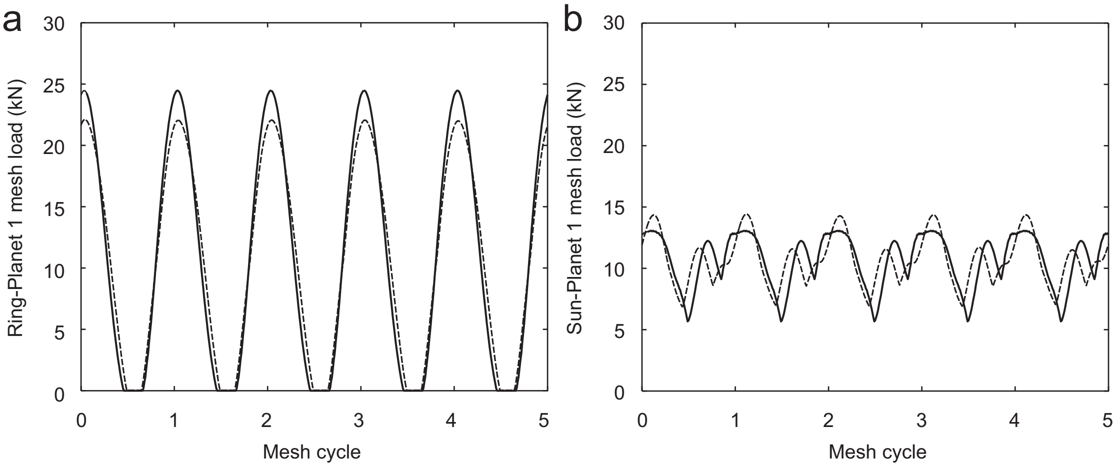

Fig. 5. Steady state (a) ring–planet 1 and (b) sun–Planet 1 mesh forces at mesh frequency 1900 Hz corresponding to the lower branch of case 1. Ring–planet 1 mesh force is dominant: (—) FE model and (- - -) analytical model.

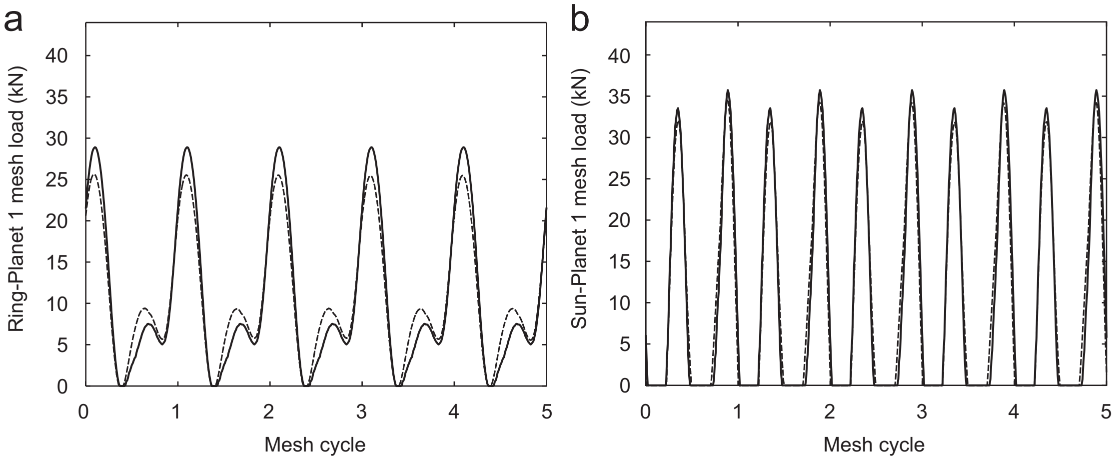

Fig. 6. Steady state (a) ring–planet 1 and (b) sun–planet 1 mesh forces at mesh frequency 1900 Hz corresponding to the upper branch of case 1. Sun–planet 1 mesh force is dominant: (—) FE model and (- - -) analytical model.

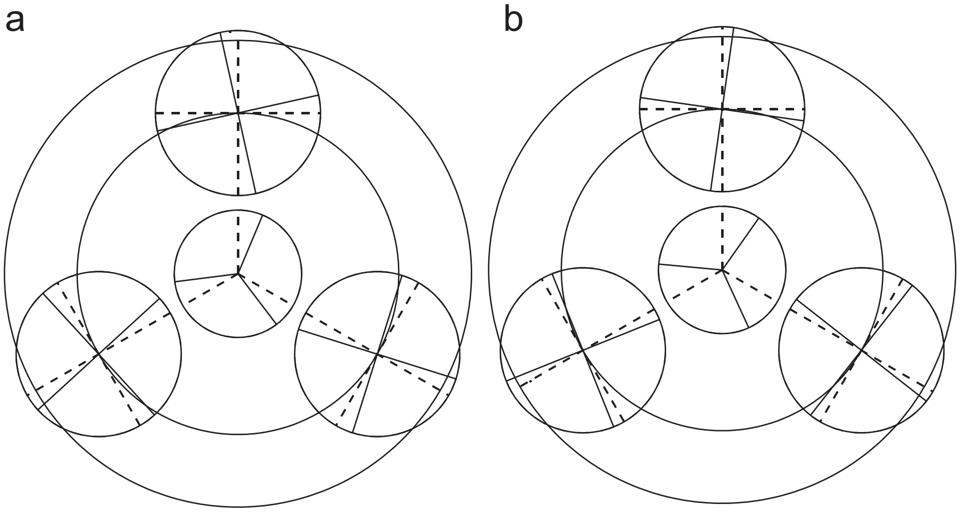

Fig. 7. Vibration modes corresponding to the distinct natural frequencies for the system of case 1 in Table 1. The ring is fixed and the carrier is constrained to zero rotational vibration: (a) mode 1 with $\omega_1 = 1846.2\,\text{Hz}$, and (b) mode 4 with $\omega_4 = 4379.8\,\text{Hz}$. (—) modal deflection and (- - -) undeformed.

of mesh frequency, so too is the rotation (or translation) of the sun, ring, and carrier in that harmonic. In planetary gears, similar to other geared systems, resonance potentially occurs when the mesh frequency or one of its harmonics equals a natural frequency ($l\omega_m \approx \omega_i$, $l = 1, 2, \ldots$). According to the mesh phasing rules in Table 4, however, certain harmonics of mesh frequency do not excite resonant response.

3.1. Jump phenomena in steady-state responses

The natural frequencies of the system in case 1 (Table 1) are obtained from the eigenvalue problem of the rotational model Eq. (3) with mean mesh stiffnesses. In Fig. 3(a) and (b) are shown the rms (mean-removed) and mean values of the steady-state sun rotation in a rotational system with three equally spaced planets (case 1, Table 1) from both the analytical and finite element models. The rms mean-removed values are calculated in the time domain; there is no omission of any spectral content. Only stable solutions are shown, as the numerical integration methods used to solve the dynamics of both models do not trace unstable solutions. The agreement between models is very good. The spectral details of the sun rotation for decreasing mesh frequency from the finite element and analytical models are shown in Fig. 4(a) and (b). The spectra generated from both models, which are a more challenging comparison than rms, agree very well.

A nonlinear jump phenomenon occurs at the primary resonance of the first distinct mode ($\omega_m \approx \omega_1 = 1846\,\text{Hz}$) as the mesh frequency is varied. Bending of the rms resonance curve to the left indicates softening nonlinearity due to the reduced system stiffness as the gears lose contact at large vibrations. The rms response jumps up as the frequency is increased and jumps down at a lower frequency when the mesh frequency is decreased. Corresponding jumps opposite in direction occur in the mean response (Fig. 3(b)). Multiple steady-state solutions are possible in the mesh frequency range between the jump up and jump down frequencies. Jumps also occur at the resonance of the second distinct mode excited by the second harmonic of mesh frequency ($2\omega_m \approx \omega_4 = 4379\,\text{Hz}$). Because $2\omega_1 \approx \omega_4$, the primary resonance corresponding to ω_1 and the second harmonic resonance corresponding to ω_4 overlap in the mesh frequency range 1800–2200 Hz. The open circles at 2350 and 2050 Hz on the lower branch of the response curve indicate the onset of gear tooth separation, which continues along the branches for increasing amplitudes.

From the mathematical form of the analytical model one concludes that the resonant behaviors are parametric instabilities from mesh stiffness fluctuation. The finite element model shows the same dynamics (Figs. 3 and 4) even though it is based on a formulation that makes no stipulation of a time-varying stiffness and is not predisposed to yield the same parametric instabilities. Thus, the finite element method provides independent confirmation of the parametrically excited structure of the analytical model.

The resonances at $\omega_m \approx 1500$ and 1100 Hz correspond to the second distinct mode (ω_4) excited by higher harmonics of mesh frequency, i.e., $3\omega_m \approx \omega_4$ and $4\omega_m \approx \omega_4$. Because $Z_s = 27$, $Z_r = 99$, and $N = 3$, the quantity $k = \text{mod}\,(lZ_s/N) = 0$ for all l. Thus, the mesh phasing rules predict that the distinct modes at natural

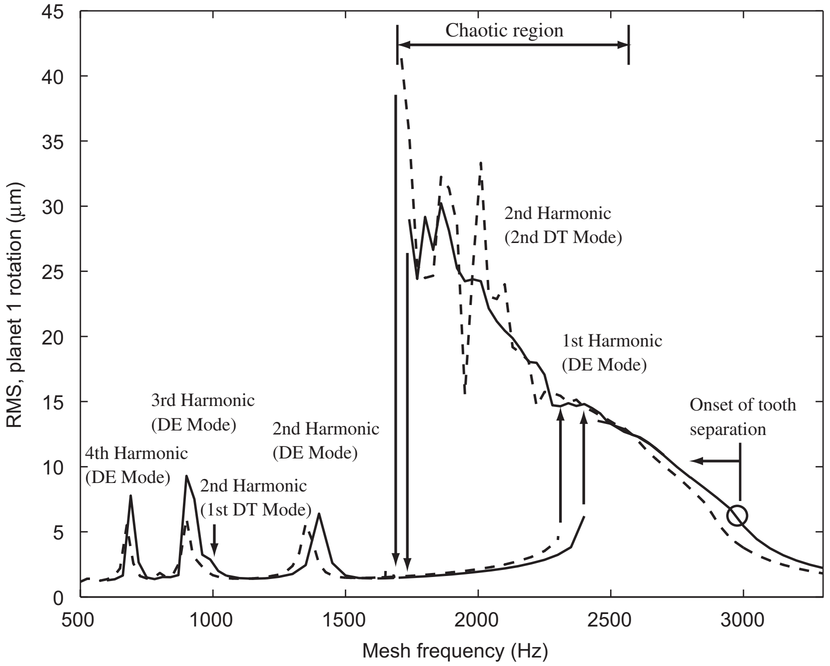

Fig. 8. Steady-state rms values (mean removed) of planet 1 rotation for increasing and decreasing speeds in finite element and analytical models for case 2. Chaos is predicted in both the models (*note*: DT Mode–distinct mode, DE–degenerate mode): (—) FE model and (- - -) analytical model.

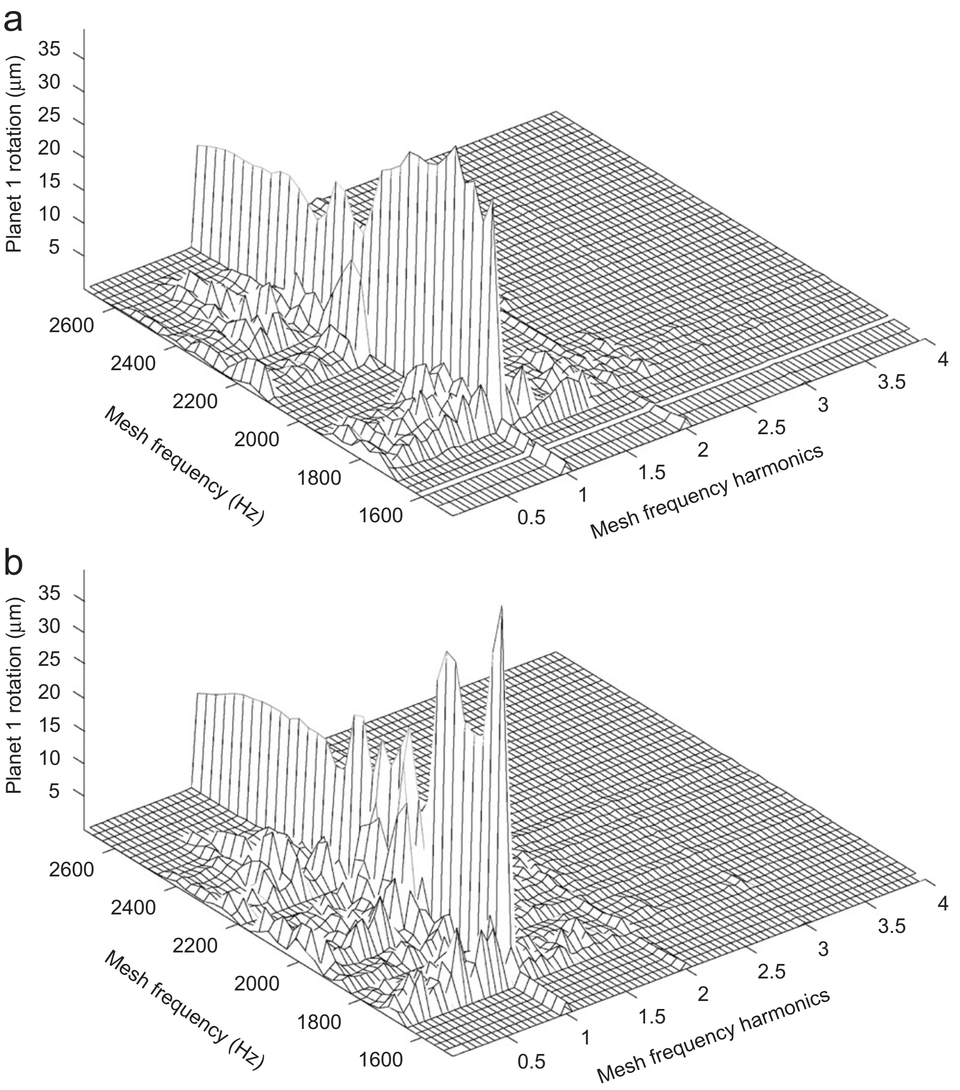

Fig. 9. Waterfall spectra of planet 1 rotation for decreasing speeds in (a) finite element and (b) analytical models for case 2. Chaos is predicted in both models.

frequencies 1846 and 4379 Hz are excited by mesh frequency and any of its higher harmonics, whereas the degenerate modes at $\omega_2 = \omega_3 = 2744$ Hz are not excited by any harmonics of mesh frequency. Consistent with these predictions, the response shows no resonance corresponding to the degenerate modes (ω_2 and ω_3).

The upper branch at 1900 Hz (Fig. 3) corresponds to the second harmonic resonance of ω_4, that is $2\omega_m \approx \omega_4$, and the lower branch corresponds to the primary resonance of ω_1, i.e., $\omega_m \approx \omega_1$. The multiple steady-state responses at mesh frequency 1900 Hz are obtained by choosing suitable initial conditions. In spite of the occurrence of tooth contact loss at 1900 Hz on the upper branch, the solution remains periodic with period T_m, as is evident from Fig. 4.

Examination of the dynamic mesh forces near various resonances indicates the source of the vibration. The sun–planet 1 and ring–planet 1 mesh forces at 1900 Hz corresponding to the lower branch for the case 1 system are shown in Fig. 5(a) and (b). The dynamic fluctuation of the ring–planet 1 mesh force is higher than that for the sun–planet 1 mesh force. In fact, the ring–planet 1 mesh loses contact even though the sun–planet 1 mesh does not. This dominance of ring–planet mesh force over sun–planet mesh force occurs at all other resonances

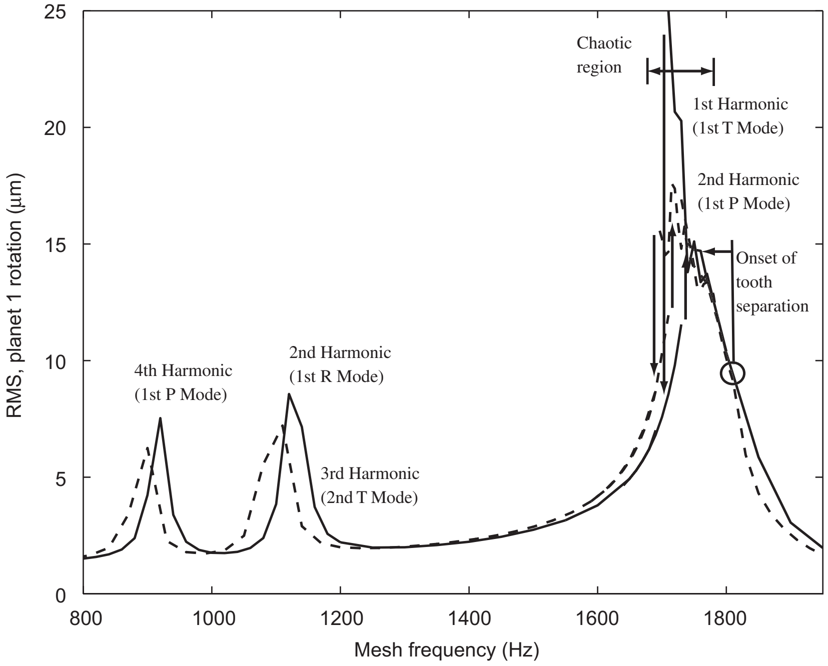

Fig. 10. Steady-state rms values (mean removed) of planet 1 rotation for increasing and decreasing speeds in finite element and analytical models for case 4 (*note*: T Mode—translational mode, R Mode—rotational mode, P Mode—planet mode): (—) FE model and (- - -) analytical model.

corresponding to the first distinct mode ω_1. In Fig. 6(a) and (b) are shown the sun–planet 1 and ring–planet 1 mesh forces at the same mesh frequency but corresponding to the upper branch. While both meshes lose contact, the dynamic fluctuation of the sun–planet 1 mesh force is higher than that for the ring–planet 1 mesh force, and the contact loss at the sun–planet 1 mesh is more pronounced than at the ring–planet 1 mesh. This dominance of sun–planet mesh force over ring–planet mesh force occurs at all other resonances corresponding to the second distinct mode ω_4. The strong agreement between the finite element and analytical mesh forces shown in Figs. 5 and 6 supports the validity of the analytical model.

The dominance of either the ring–planet or sun–planet mesh forces at a given resonance is directly related to the resonant vibration mode. Dynamic mesh forces are approximately proportional to the mesh deflections of the dominant resonant mode. For the first distinct mode (ω_1) the mesh deflection at a ring–planet mesh is greater than the mesh deflection at a sun–planet mesh (Fig. 7(a)), resulting in larger mesh forces at the ring–planet meshes than at the sun–planet meshes. For the second distinct mode the mesh deflection at a sun–planet mesh exceeds the mesh deflection at a ring–planet mesh (Fig. 7(b)), resulting in dominance of the sun–planet mesh forces.

3.2. Chaotic response

The rms values (mean-removed) of the planet 1 rotation at various speeds for a rotational system with four diametrically opposed planets (case 2, Table 1) are shown in Fig. 8. The natural frequencies of the system are in Table 1. Jump phenomena for increasing and decreasing speeds occur near the primary resonance of the first degenerate mode ($\omega_m \approx \omega_4 = 2860\,\text{Hz}$), as indicated by the arrows in Fig. 8. The distinctive feature in this case is the chaotic response along the upper branch for decreasing speed between 2600 and 1700 Hz. Other resonant modes might also have been excited in the ensuing chaotic response for decreasing speeds. The broadband spectra in the waterfall plot from both the analytical and finite element models for decreasing speeds in Fig. 9(a) and (b) show that the motion is chaotic. Chaotic response is also observed in the spur gear pair experiments of Kahraman and Blankenship [1]. Chaotic motion does not occur for the lower branch

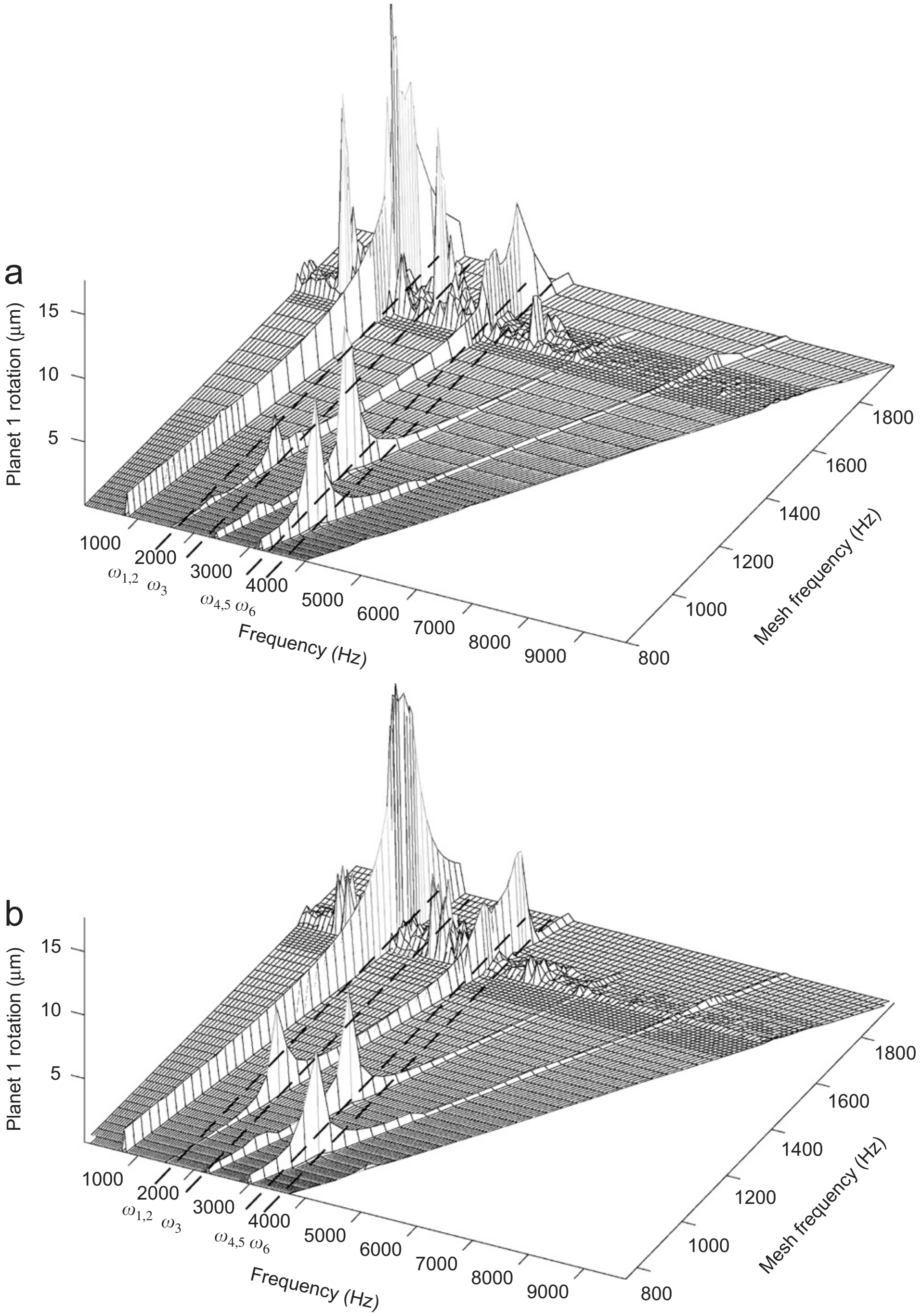

Fig. 11. Waterfall spectra of planet 1 rotation for decreasing speeds in (a) finite element and (b) analytical models of case 4. Chaos is predicted in both the models in the mesh frequency range of 1780–1700 Hz.

corresponding to increasing speed. The analytical and finite element results agree well in both rms values and detailed spectra except in the chaotic regions where the details of the chaotic attractors differ. This is not unexpected as the attractors are likely sensitive to the model, and the two models are based on different foundations with different modeling refinement. The speeds at which chaos occurs match between the models.

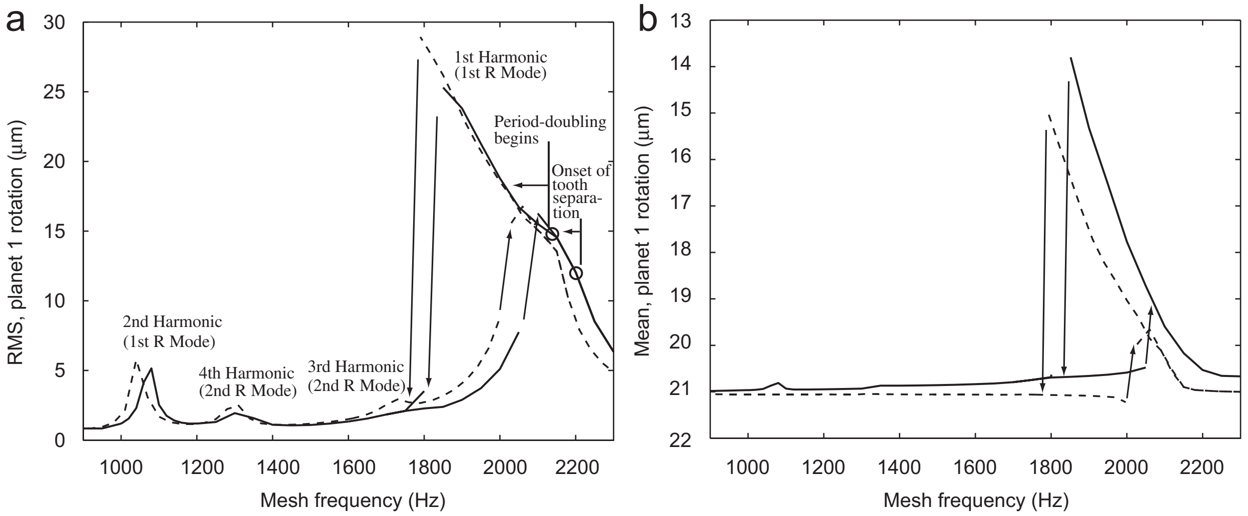

Fig. 12. Steady-state (a) rms (mean removed) and (b) mean values of planet 1 rotation for increasing and decreasing speeds in finite element and analytical models of case 3 (*note*: R Mode—rotational mode): (—) FE model and (- - -) analytical model.

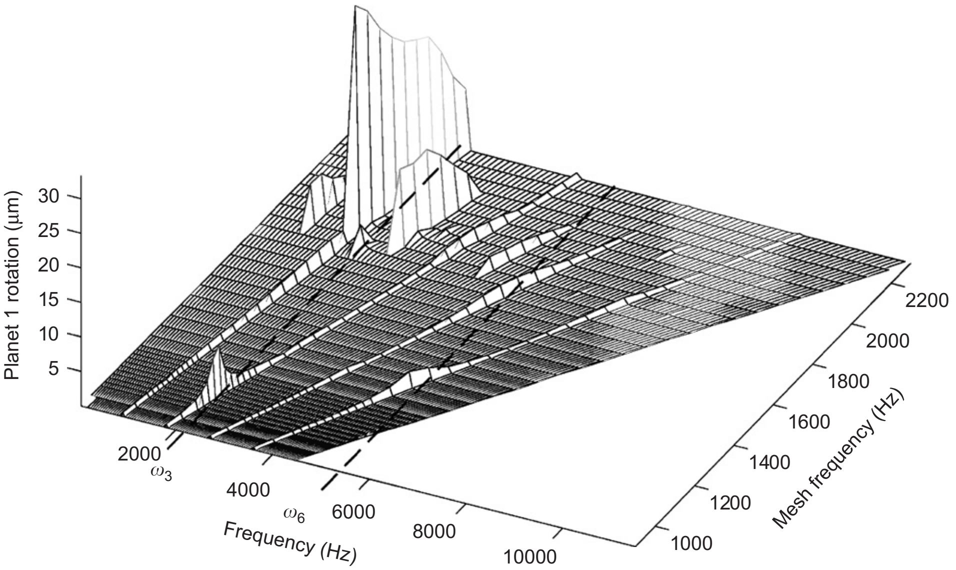

Fig. 13. Waterfall spectra of planet 1 rotation for decreasing speeds in the finite element model of case 3. Period-doubling bifurcation is predicted in the finite element and analytical models.

In the non-chaotic regions, according to the mesh phasing rules in Table 4, degenerate modes are excited by all harmonics of mesh frequency and distinct modes are excited only by even harmonics. Resonances near mesh frequencies of 1350, 850, and 690 Hz correspond to the degenerate modes excited by higher harmonics of mesh frequency and the very small resonance peak near 1000 Hz corresponds to the first distinct mode excited by the second harmonic of mesh frequency.

In Fig. 10 is shown the planet 1 rotation of a system with four diametrically opposed planets with flexible bearings (case 4, Table 1). This system includes rotational and translational degrees of freedom of the planetary gear components. The first few natural frequencies are in Table 1. The response corresponding to the upper branch (decreasing speed) near primary resonance of the first translational mode

($\omega_m \approx \omega_1 = 1766$ Hz) becomes chaotic in the mesh frequency range 1780–1700 Hz. This is evident from the distributed, broadband spectra of the response for decreasing speed shown in the waterfall plots in Fig. 11 from the analytical and finite element models. In the waterfall spectra a resonance peak at 1720 Hz corresponding to the closely spaced translational modes at $\omega_4 \approx \omega_5$ in the chaotic region is excited by the second harmonic of the mesh frequency. While this should not be possible based on mesh phasing rules, the mesh phasing rules derived based on periodicity of planetary gear mesh forces are not valid during chaotic motions. Both models capture this deviation, and agreement of the spectra is good throughout the analyzed range except where chaos occurs (although the speeds where chaos occurs also match).

3.3. Period-doubling bifurcation

Period-doubling bifurcations are a route to chaos in clearance-type nonlinear systems when system parameters such as peak–peak dynamic forces/mesh stiffness variations or damping are changed [31]. This type of behavior appears to occur in planetary gears as well, where the nonlinearity is of clearance-type. In Fig. 12 is shown the rms (mean-removed) and mean steady-state response of planet 1 rotation for a system with three equally spaced planets with flexible bearings (case 3, Table 1). The first few natural frequencies are in Table 1. Spectral details of the finite element response are shown in Fig. 13. The analytical model spectra agree well with comparison equal to that in Fig. 4. Note the open circle at 2200 Hz in the response curve of Fig. 12(a). This delineates the boundary of contact loss (of the ring–planet meshes for this system). Another open circle at 2150 Hz indicates a sudden period-doubling in the response as the mesh frequency is decreased. Period-doubling is evident in the waterfall spectra in Fig. 13 where response of half-orders of mesh frequency is present. Response at half of mesh frequency is common in geared systems when the mesh frequency or one of its harmonics is nearly twice a natural frequency ($l\omega_m \approx 2\omega_i$). Such behavior is explained by linear theory where the time-varying mesh stiffness at frequency $l\omega_m$ excites parametric instability of the ith mode [16]. In contrast, the period-doubling in Fig. 13 is truly nonlinear. To determine whether the response is a parametric resonance caused by the second harmonic of mesh frequency, a simulation using the analytical model without any of the higher harmonics in the mesh stiffnesses variation is conducted. The response is still period-$2T_m$. Hence this is not a parametric instability but a period-doubling bifurcation near primary resonance ($\omega_m \approx \omega_3$).

When the amplitude of the first harmonic of mesh stiffness variation at all meshes is doubled, keeping the rest of system parameters the same, chaos is observed at the mesh frequency of 1900 Hz corresponding to the upper branch. The Poincaré map in Fig. 14(a) and the unrepeating time history of planet 1 rotation in Fig. 14(b) confirm that the response is chaotic. The solution turns to period-T_m when the amplitude of the first harmonic of all mesh stiffnesses is halved. Thus from our observations of the transition of period-T_m solution

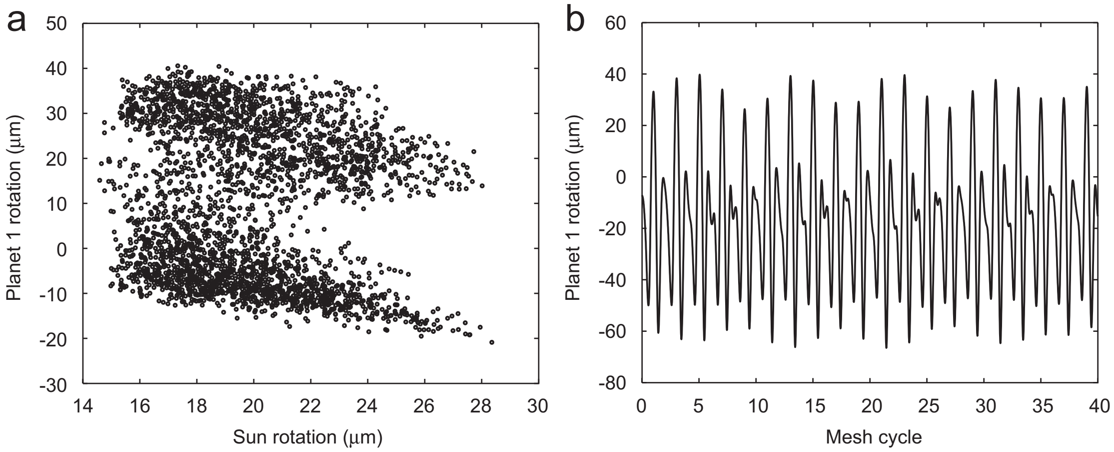

Fig. 14. Steady-state (a) Poincaré map and (b) time response at 1900 Hz corresponding to the upper branch of case 3 (Fig. 12) when the amplitude of first harmonic of the mesh stiffness variation is doubled. The Poincaré section sampled at $t = 0$, T_m, $2T_m$, … is shown by open circles. The period-doubling response leads to chaos.

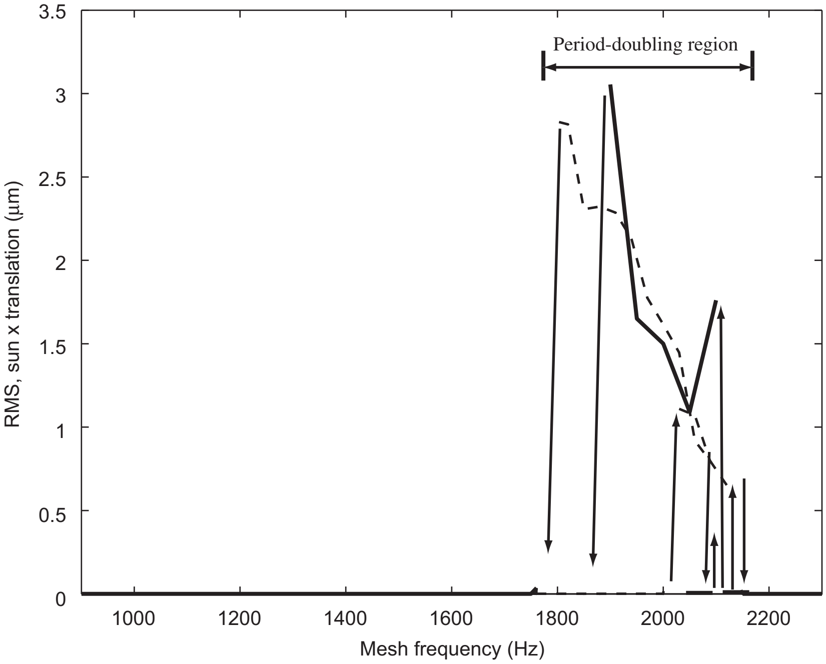

Fig. 15. Steady-state rms (mean removed) response of sun translation for increasing and decreasing speeds in finite element and analytical models of case 3. Note that the response is zero at all regions in accordance with mesh phasing conclusions except in the period-doubling region: (—) FE model and (- - -) analytical model.

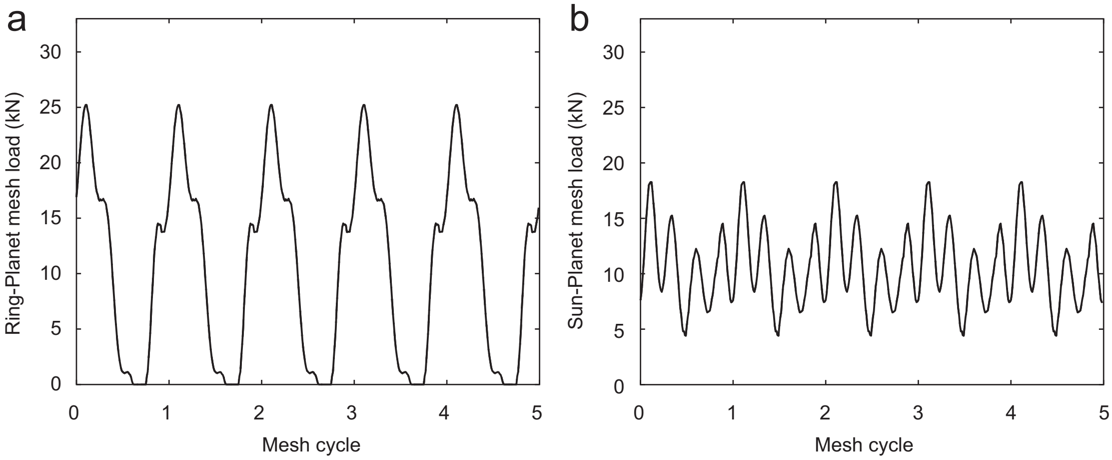

Fig. 16. Steady-state (a) ring–planet and (b) sun–planet mesh forces at all the three planet meshes of case 3 at mesh frequency 2150 Hz. Symmetry of the system ensures equal forces on all planets, and all three curves overlap in both figures: (—) planet 1 mesh, (- - -) planet 2 mesh, and (…) planet 3 mesh.

to period-$2T_m$ and finally to chaos with increasing amplitudes of mesh stiffness variation we hypothesise that this is an occurrence of period-doubling bifurcation leading to chaos. Period-$4T_m$ and period-$8T_m$ solutions would better establish the period-doubling route to chaos, but such solutions were not observed for this example system.

Similar to the chaotic regions, mesh phasing rules do not apply in the period-doubling regions. According to the mesh phasing rules in Table 4, sun translations should not be excited for the present system (case 3).

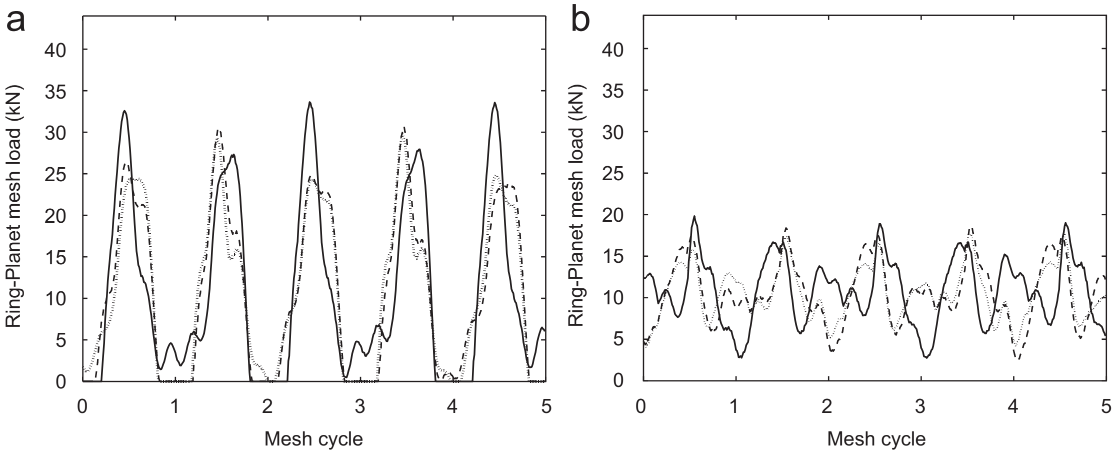

Fig. 17. Steady-state (a) ring–planet and (b) sun–planet mesh forces at mesh frequency 1900 Hz corresponding to the upper branch of case 3. The mesh forces are not identical at all the planets due to the period-doubling bifurcation: (—) planet 1 mesh, (- - -) planet 2 mesh, and (…) planet 3 mesh.

In Fig. 15 it is shown that sun translation, however, is excited in the period-doubling region but remains zero (as anticipated) in other regions. Because of the identical relative positioning and mesh phase of all three planets (symmetry) in the present system (case 3), the dynamic forces at all sun–planet meshes are the same at all ring–planet meshes. In Fig. 16 the ring–planet and sun–planet mesh forces at 2150 Hz are shown. Even though ring–planet tooth separation occurs at this mesh frequency, the dynamic mesh forces at all the three ring–planet and sun–planet meshes remain identical and T_m-periodic, in accordance with the mesh phasing analysis [18–20]. Mesh forces at 1900 Hz on the upper branch in the period-doubling region, however, are not identical and are $2T_m$-periodic (Fig. 17). In the period-doubling region the period-T_m solution exists but might be unstable bifurcating to a period-$2T_m$ solution. The symmetry of the system is lost, as shown in Fig. 17. Periodicity and symmetry of mesh forces are key assumptions in deriving mesh phasing rules, so deviation from these rules in chaotic and period-doubling regions is natural.

4. Conclusions

In this paper two independent models: one a lumped-parameter mathematical model and the other a finite element model, with different formulations and different mesh modeling assumptions are used to analyze the nonlinear dynamics of planetary gears. The main conclusions are:

(1) There is strong agreement between the analytical and finite element model's responses across a range of complicated nonlinear behaviors for different planetary gear configurations; this confirms the validity of the lumped-parameter model for predicting planetary gear dynamics.
(2) Resonances occur due to parametric instabilities from mesh stiffness fluctuation. The bending of resonance curves to the left indicate softening-type nonlinearity due to tooth contact loss. Jumps occur near primary and higher harmonic resonances due to multiple steady-state solutions in these regions.
(3) Other nonlinear phenomena common in systems having clearance-type nonlinearities such as chaos and period-doubling bifurcation are predicted by both models. The occurrence of chaos stresses the need to model tooth contact loss nonlinearity in planetary gears.
(4) The mesh phasing rules, derived based on the periodicity and the symmetry of mesh forces, are valid even when tooth contact loss occurs. Chaos or period-doubling bifurcations, however, disturb the symmetry in planetary gears. Hence, mesh phasing rules are not valid in these regions.
(5) The dominance of either the sun–planet or ring–planet mesh forces at a given resonance is directly related to the mesh deflection in that particular resonant mode.

Acknowledgements

The authors thank Dr. Sandeep M. Vijayakar of Advanced Numerical Solutions, Inc. for his guidance and for providing the Calyx finite element software package for gear dynamics.

References

[1] A. Kahraman, G.W. Blankenship, Experiments on nonlinear dynamic behavior of an oscillator with clearance and periodically time-varying parameters, *Journal of Applied Mechanics* 64 (1997) 217–226.

[2] G.W. Blankenship, A. Kahraman, Steady state forced response of a mechanical oscillator with combined parametric excitation and clearance type non-linearity, *Journal of Sound and Vibration* 185 (5) (1995) 743–765.

[3] M. Botman, Vibration measurements on planetary gears of aircraft turbine engines, *Journal of Aircraft* 17 (5) (1980) 351–357.

[4] F. Cunliffe, J.D. Smith, D.B. Welbourn, Dynamic tooth loads in epicyclic gears, *ASME Journal of Engineering for Industry* (1974) 578–584.

[5] M. Botman, Epicyclic gear vibrations, *ASME Journal of Engineering for Industry* (1976) 811–815.

[6] T. Hidaka, Y. Terauchi, Dynamic behaviour of planetary gear (1st report: load distribution in planetary gear), *Bulletin of the JSME-Japan Society of Mechanical Engineers* 19 (132) (1976) 690–698.

[7] T. Hidaka, Y. Terauchi, K. Ishioka, Dynamic behaviour of planetary gear (2nd report: displacement of sun gear and ring gear), *Bulletin of the JSME-Japan Society of Mechanical Engineers* 19 (138) (1976) 1563–1570.

[8] T. Hidaka, Y. Terauchi, M. Nohara, J. Oshita, Dynamic behaviour of planetary gear (3rd report: displacement of ring gear in direction of line of action), *Bulletin of the JSME-Japan Society of Mechanical Engineers* 20 (150) (1977) 1663–1672.

[9] A. Kahraman, Planetary gear train dynamics, *Journal of Mechanical Design* 116 (3) (1994) 713–720.

[10] A. Kahraman, Natural-modes of planetary gear trains, *Journal of Sound and Vibration* 173 (1) (1994) 125–130.

[11] A. Kahraman, Load sharing characteristics of planetary transmissions, *Mechanism and Machine Theory* 29 (8) (1994) 1151–1165.

[12] J. Lin, R.G. Parker, Analytical characterization of the unique properties of planetary gear free vibration, *Journal of Vibration and Acoustics* 121 (3) (1999) 316–321.

[13] J. Lin, R.G. Parker, Structured vibration characteristics of planetary gears with unequally spaced planets, *Journal of Sound and Vibration* 233 (5) (2000) 921–928.

[14] J. Lin, R.G. Parker, Sensitivity of planetary gear natural frequencies and vibration modes to model parameters, *Journal of Sound and Vibration* 228 (1) (1999) 109–128.

[15] J. Lin, R.G. Parker, Natural frequency veering in planetary gears, *Mechanics of Structures and Machines* 29 (4) (2001) 411–429.

[16] J. Lin, R.G. Parker, Planetary gear parametric instability caused by mesh stiffness variation, *Journal of Sound and Vibration* 249 (1) (2002) 129–145.

[17] A. Kahraman, G.W. Blankenship, Planet mesh phasing in epicyclic gear sets, *Proceedings of International Gearing Conference*, Newcastle, 1994, pp. 99–104.

[18] R.G. Parker, A physical explanation for the effectiveness of planet phasing to suppress planetary gear vibration, *Journal of Sound and Vibration* 236 (4) (2000) 561–573.

[19] V.K. Ambarisha, R.G. Parker, Suppression of planet mode response in planetary gear dynamics through mesh phasing, *ASME Journal of Vibration and Acoustics* 128 (2006) 133–142.

[20] R.G. Parker, J. Lin, Mesh phasing relationships in planetary and epicyclic gears, *Journal of Mechanical Design* 126 (2004) 365–370.

[21] P. Velex, L. Flamand, Dynamic response of planetary trains to mesh parametric excitations, *ASME Journal of Mechanical Design* 118 (1996) 7–14.

[22] R.G. Parker, S.M. Vijayakar, T. Imajo, Non-linear dynamic response of a spur gear pair: modeling and experimental comparisons, *Journal of Sound and Vibration* 237 (3) (2000) 435–455.

[23] R.G. Parker, V. Agashe, S.M. Vijayakar, Dynamic response of a planetary gear system using a finite element/contact mechanics model, *Journal of Mechanical Design* 122 (3) (2000) 304–310.

[24] A. Kahraman, S.M. Vijayakar, Effect of internal gear flexibility on the quasi-static behavior of a planetary gear set, *Journal of Mechanical Design* 123 (3) (2001) 408–415.

[25] A. Kahraman, A.A. Kharazi, M. Umrani, A deformable body dynamic analysis of planetary gears with thin rims, *Journal of Sound and Vibration* 262 (2003) 752–768.

[26] C. Yuksel, A. Kahraman, Dynamic tooth loads of planetary gears sets having tooth profile wear, *Mechanisms and Machine Theory* 39 (2004) 695–715.

[27] S.M. Vijayakar, *Calyx user's Manual* 〈http://ansol.com〉.

[28] S.M. Vijayakar, A combined surface integral and finite element solution for a three-dimensional contact problem, *International Journal for Numerical Methods in Engineering* 31 (1991) 524–546.

[29] S.M. Vijayakar, H.R. Busby, D.R. Houser, Linearization of multibody frictional contact problems, *Computers and Structures* 29 (1988) 569–576.

[30] X. Wu, R.G. Parker, Modal properties of planetary gears with an elastic continuum ring gear, *ASME Journal of Applied Mechanics* (2006), submitted for publication.

[31] A. Kahraman, On the response of a preloaded mechanical oscillator with a clearance: period-doubling and chaos, *Nonlinear Dynamics* 3 (1992) 183–198.